JOURNAL OF MATERIALS SCIENCE: MATERIALS IN MEDICINE 10 (1999) 191–198

The implant material, Ti6Al7Nb: surface microstructure, composition and properties

C. SITTIG, G. HÄHNER, A. MARTI‡, M. TEXTOR, N. D. SPENCER*
Laboratory for Surface Science and Technology, Department of Materials, ETH Zürich, Sonneggstr. 5, CH - 8092 Zürich, Switzerland

R. HAUERT
Swiss Federal Laboratories for Materials Testing and Research, Überlandstr. 129, CH-8600 Dübendorf, Switzerland

The excellent biocompatibility of titanium and its alloys is intimately related with the properties of the surface in contact with the biological environment, and therefore it is closely connected with the stable, passivating oxide layer that forms on its surface. In the present paper, the oxide layer on the alloy Ti6Al7Nb has been characterized using X-ray photoelectron spectroscopy, scanning Auger microscopy and pH-dependent lateral force microscopy. The alloying elements Al and Nb are incorporated in the oxide layer and detected in their most stable oxidized form, as Al_2O_3 and Nb_2O_5. Their distribution in the oxide reflects the underlying α-β microstructure, with enrichment of Al in the α- and of Nb in the β-phase (determined by electron microprobe). Friction measurements (lateral force microscopy) indicate slightly different, pH-dependent, lateral forces above the α- and β-phase structures that point to small local variations in surface charges.

1. Introduction

Titanium and its alloys are among the most commonly used implant materials [1–3], particularly for dental, orthopaedic and osteosynthesis applications. The interaction of the implant with its biological environment, the formation of the foreign material/tissue interface and the long-term success or failure of integration in the body is strongly connected with the surface properties of the implant device [4] – in the case of titanium, with the oxide layer. On the molecular level, the physical and chemical properties of the implant surface, e.g. structure, defects, roughness, contamination layer, surface energy and surface charges [5, 6], are highly significant in determining the type and degree of surface/biomolecule interactions [7]. One of several factors that determine the adsorption kinetics of proteins on surfaces is the electrochemical behavior of the titanium oxide [8–10].

Surface charges on biomaterial surfaces (metals, oxides and polymers) have been shown to influence surface properties that are relevant to the biocompatibility of the materials. This is particularly true for anchorage-dependent cells such as osteoblasts, where surface charges affect the attachment, morphology, migration and phenotype expression of cells *in vitro* [11]. The attachment and spreading of osteoblast cells is reported to be extraordinarily strong on very positively charged surfaces, with very intimate contact between the ventral cell membrane and the biomaterial surface. On negatively charged surfaces on the other hand, osteoblast cells tend to show a stand-off morphology with very localized attachment points [12]. It is very likely that this is an indirect effect of the biomaterial surface charges on cell behavior, the surface charges influencing the protein population and the conformation of the adsorbed proteins through electrostatic interaction. The type and conformation of the adsorbed proteins, in turn, triggers osteoblast behavior such as adhesion, migration, spreading, proliferation and differentiation of the cells.

The heterogeneous Ti6Al7Nb (wt %) alloy has an α-β structure [13], where the Al is enriched in the α-phase, while Nb is enriched in the β-phase. To what extent the metal microstructure influences the local composition and morphology of the oxide overlayer was not studied in detail prior to the current investigation. In this study, the microstructure of the native oxide layer on Ti6Al7Nb has been investigated with X-ray photoelectron spectroscopy (XPS), scanning Auger microscopy (SAM) and atomic/lateral force microscopy (AFM/LFM). The latter technique, when performed in aqueous electrolyte solution at different pH values, has been shown to be a promising method for the analysis of local surface charge differences on oxide films [14, 15]. Differences in the oxide layer of Ti6Al7Nb and commercial pure (cp) Ti may contribute to an understanding of differences in the biological response to these two implant materials.

*To whom correspondence should be addressed. Email: nspencer@surface.mat.ethz.ch.
‡Present address: Robert Mathys Stiftung, Bischmattstr. 12, CH-2544 Bettlach, Switzerland.

2. Materials and methods

2.1. Material and surface preparation

Ti6Al7Nb discs were cut from a 16 mm rod. The samples were cleaned and then annealed (900 °C, 4 h, in air) in order to slightly coarsen the microstructure (Fig. 1) for easier analytical imaging. The oxide layer, formed during annealing, was removed by grinding (SiC paper). Then the surfaces were mechanically polished to a mirror finish, using SiC grinding paper down to grit size 600 (15 μm particle diameter), and then polished with 10 μm diamond paste in oil and finally with a 0.06 μm SiO_2 suspension. After polishing, the surfaces were cleaned in the following way: (1) successive ultrasonic cleaning in hexane, acetone, ethanol and ultrapure water (EASYpure UV, Barnstead, 18.2 MΩcm); (2) passivation in 30% HNO_3 for 1 h; (3) immersion in ultrapure water and drying with N_2; (4) plasma cleaning in O_2 plasma (Harrick PDC-32G) (at 42 Pa, for 2 min); and (5) storage in ultrapure water for at least 2 h. The samples that were investigated with LFM were cleaned with the cleaning procedure steps 1–3 only, since a certain instability in the LFM-signal was noticed following plasma treatment. It is believed that the surface is not significantly changed during plasma cleaning, which mainly removes the organic contamination [16], but a possible explanation for the LFM instability is that the equilibrium surface hydroxyl concentration is disturbed after exposure to oxygen plasma. No further growth in the 4–6 nm thickness oxide layer was observed due to plasma cleaning.

Samples prepared as described above have a microstructure that is large enough to be imaged with laterally resolving techniques such as electron microprobe (EMP) for the metal microstructure and SAM for the native oxide film.

2.2. Experimental methods

The bulk composition and microstructure were analyzed and determined (Fig. 1) by the supplier, Sulzer Orthopedics, CH-8404 Winterthur.

2.2.1. Electron microprobe

The elemental distribution in the alloy was determined by EMP measurements with a Cameca SX 100 system, operating the electron beam at 15 kV/60 nA.

2.2.2. X-ray photoelectron spectroscopy

XPS spectra were recorded with a SAGE 100 system (Specs, Berlin, Germany) using non-monochromatized AlK_α radiation at 390 W (13 kV) and an electron detector pass energy of 50 eV for survey and 14 eV for high-resolution scans. Measurements were made at a take-off angle of 90° with respect to the sample surface. The area of information is typically $9 \times 9\,mm^2$, the results therefore represent a laterally averaged chemical composition. To determine the quantitative surface composition from XPS data, the sensitivity factors of Evans *et al*. [17] were used. All binding energies were referenced by setting the CH_x peak to 285 eV.

2.2.3. Scanning Auger microscopy

SAM measurements were performed to investigate the lateral distribution of the alloying elements in the oxide layer (information depth: 3–5 nm). They were carried out with a Physical Electronics PHI 4300 SAM system, operating the electron beam at 8 kV/85 nA and the cylindrical mirror analyzer at 0.3% resolution. The lateral resolution of the SAM system is about 0.1 μm.

2.2.4. Lateral force microscopy

To investigate differences in surface charging of the two different surface phases (detected by SAM analysis), LFM measurements were performed using an AFM/LFM (Nanoscope III, Digital Instruments, Santa Barbara, CA), fitted with a liquid cell. The nominal spring constant of the commercially available Si_3N_4 cantilever used was $0.03\,N\,m^{-1}$ (Park Scientific Instruments, Sunnyvale, CA). Prior to the measurement, the cantilevers were plasma cleaned in an O_2 atmosphere for 2 min. The frictional force measurements were performed with a 125-μm scanner. The frictional force was determined by calculating the difference of the lateral signal between forward and backward scanning [15]. The applied load was typically 2 nN, and it was checked immediately following the scan (by means of a force curve measurement), in order to ensure its constancy during the friction experiments. The electrolyte used was a 10 mM aqueous NaCl solution (Fluka Chemie AG), where the pH values were adjusted with HCl in the acid range and NaOH (Merck AG) in the alkaline range, choosing appropriate acid or base concentration in order to maintain a nearly constant ionic strength. The H_3O^+ concentration of the aqueous electrolyte solution was monitored with a pH meter (Mettler, Delta 340). The pH values used in this work ranged from 3.8 to 7.9.

3. Results and discussions

3.1. Microstructure

The microstructure before annealing (Fig. 1a) clearly shows the expected duplex microstructure consisting of the so called α- and β-phases [13]. Al stabilizes the low-temperature α-phase (h.c.p.), while Nb stabilizes the high-temperature β-phase (b.c.c.). The latter phase thus contains a higher concentration of Nb, whereas Al is enriched in the α-phase. The resulting microstructure of this alloy can be described as grains consisting of pure α-phase surrounded by a mixture of α- and small amounts of β-phases.

The effect of the annealing at 900 °C in air for 4 h is illustrated in Fig. 1b. Both the α- and the β-phases are clearly coarsened. The α-phase grain size is in the range 5–20 μm in diameter and the β-phase grains have a size of about $1–5 \times 10–20\,\mu m^2$.

3.2. Electron microprobe

The EMP images are presented in Fig. 2. The EMP technique has an information depth of typically 3–5 μm, i.e. about half a ''grain-layer'' is investigated. These measurements demonstrate that the elemental distribu-

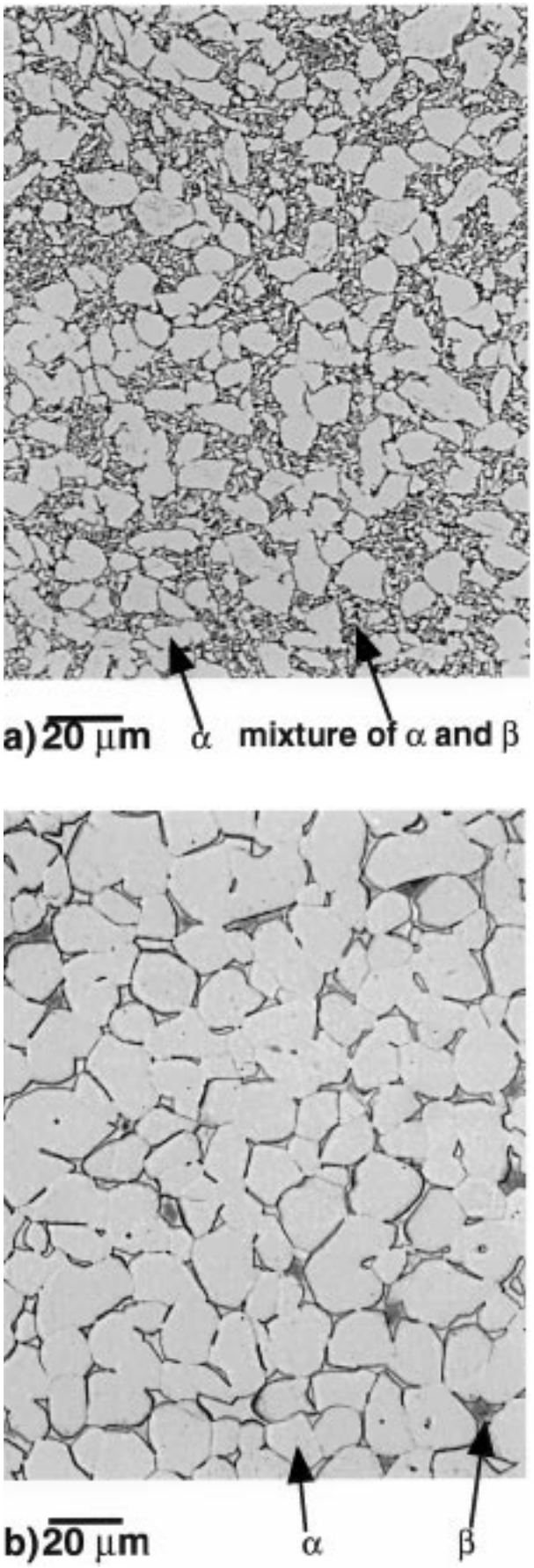

Figure 1 Microstructure of Ti6A17Nb (a) before and (b) after annealing in air (900 °C, 4 h).

tion of Ti, Al and Nb in the bulk is as expected with Al enriched grains (α-phases) and Nb enriched β-phases.

3.3. X-ray photoelectron spectroscopy

With XPS the following elements were detected at the sample surface: Ti, Al, Nb, O and C (Table I). The spectrum is dominated by Ti and O emission intensities due to the naturally formed TiO_2 surface layer. Additionally, from the Al 1s signal at 74.5 eV and the Nb 3d at 207.6 eV peak position we conclude that the alloying elements are present in the oxide film in their most stable oxidation states, i.e. as Al_2O_3 and Nb_2O_5.

If the XPS Ti (2p) signal contains a contribution from the metal below the surface oxide (with XPS using the Al-anode, 95% of the information originates from a depth of 0–7 nm in the case of TiO_2), the thickness of the oxide layer can be calculated, with the assumption of a uniformly thick and flat layer [18]. For samples prepared as described in the experimental section, the native oxide layer is calculated to have a thickness of 4–7 nm.

The calculated Ti-, Al- and Nb- surface concentrations (wt%) (normalized to 100%) are in the ratio Ti : Al : Nb = 86.1 ± 0.7 : 6.7 ± 0.8 : 7.2 ± 0.7. A comparison of these values with the concentration in the bulk (wt%) (Ti : Al : Nb = 86.6 : 6.2 : 7.2) shows that the surface concentration is similar to that of the bulk for all elements.

Furthermore, these data show that the surfaces are clean. The contamination consists mostly of carbon (about 10 at %), typically due to adsorbed organic molecules, generally present on air-exposed samples.

3.4. Scanning Auger microscopy

In contrast to EMP, SAM only senses the oxide layer. The SAM images clearly show an inhomogeneous distribution of Ti, Al and Nb (Fig. 3b, c, d) in the oxide layer, influenced by the underlying microstructure. The exact quantification of the composition in the two regions detected is difficult to determine with Auger microscopy, mainly due to changes of the O-content with measuring time (partial decomposition of the oxides during the electron bombardment). It can be said, however, that in the oxide above the α-phase the Al concentration is about two times and the Nb concentration is about 1/6 times the concentration measured above the β-phase.

The β-phase is harder than the α-phase. On polished samples, this results in a topographical structure on the surfaces, as can be seen in the secondary electron image (Fig. 3a), with the β-phases protruding slightly out of the

TABLE I XPS data [at%] of cleaned Ti6Al7Nb sample surfaces

Elements	at %
Ti	25.5 ± 0.2
Al	3.5 ± 0.4
Nb	1.1 ± 0.1
O	59.4 ± 0.1
C	10.2 ± 0.6

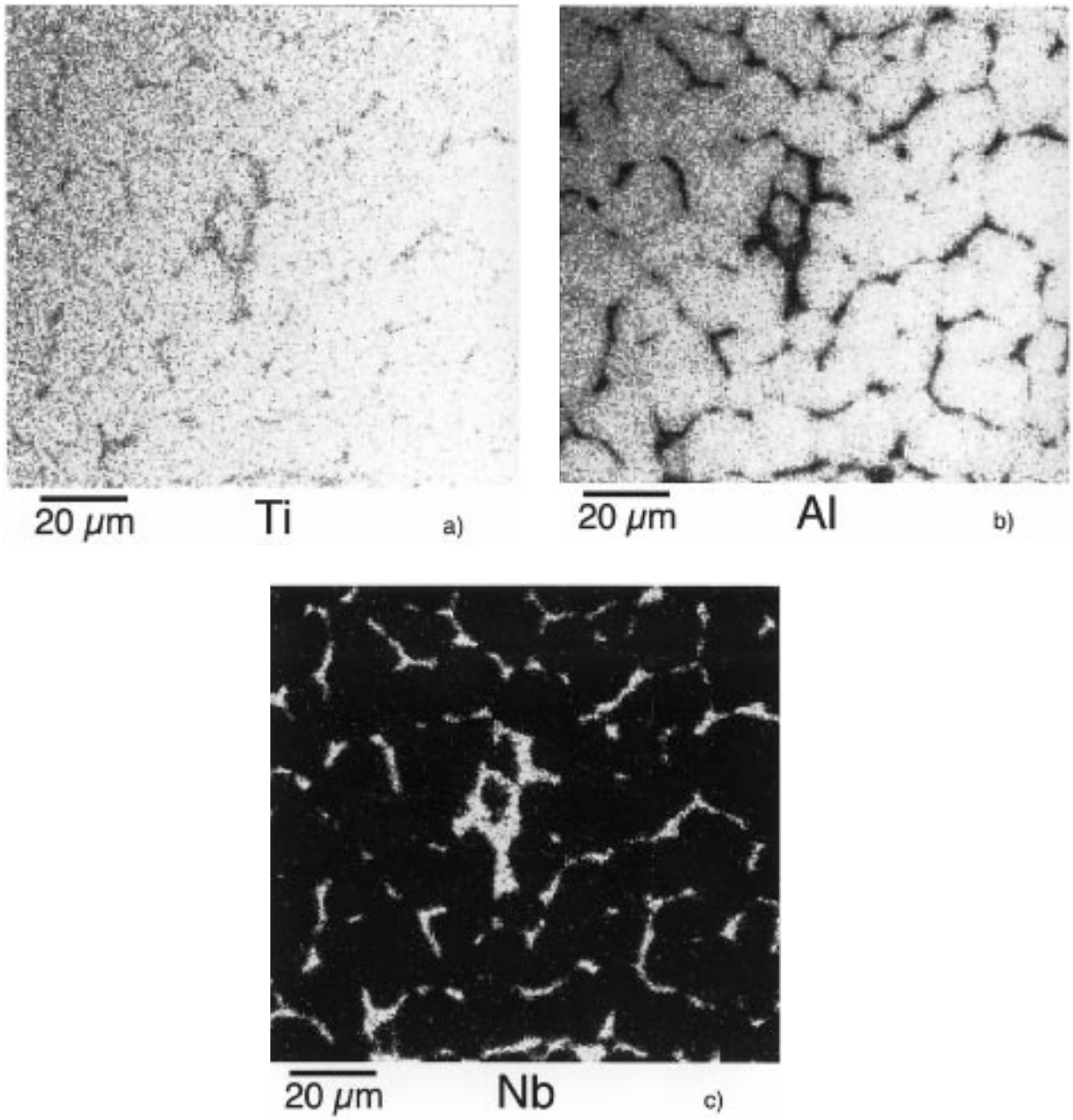

Figure 2 EMP images of the coarse grain Ti6A17Nb (information depth: 3–5 μm); the elemental distribution maps of (a) Ti, (b) Al and (c) Nb in the metal.

surface compared to the α-phases. The measured elemental distribution images are not disturbed by a topographical effect, however, as can be seen on the SAM map of C (Fig. 3e), showing an equal distribution of C on both phases.

These measurements demonstrate that the oxide layer on Ti6A17Nb is not a homogeneous layer. The alloying elements are included in the oxide layer and distributed according to the underlying metal microstructure. Therefore the oxide layers present on cp Ti (which contains neither Al_2O_3 nor Nb_2O_5) and Ti6Al7Nb are clearly different.

3.5. Lateral force microscopy

Lateral force measurements were performed in 10 mM NaCl solution as a function of pH, to investigate differences in tip-surface interactions above the two oxide phases, as detected by SAM. If the outermost surface layers of these oxide phases are distinguishable by pH-dependent LFM, local differences in the charge density distributions above the α- and β- phase are present.

Initially, AFM height images were taken to locate an area containing both oxides above the α- and the β-phase. The oxides above the α- and β-phase are distinguishable in the height image mode due to the small height differences of the two metallurgical phases occuring after polishing. Furthermore, the size of the oxide phases detected by AFM corresponds to the typical form and size of the α- and β-phases detected with SAM.

Fig. 4 shows the friction force images measured at different pH values, varying from pH 3.8 to 7.9. The friction force images are reversible in this pH range, and

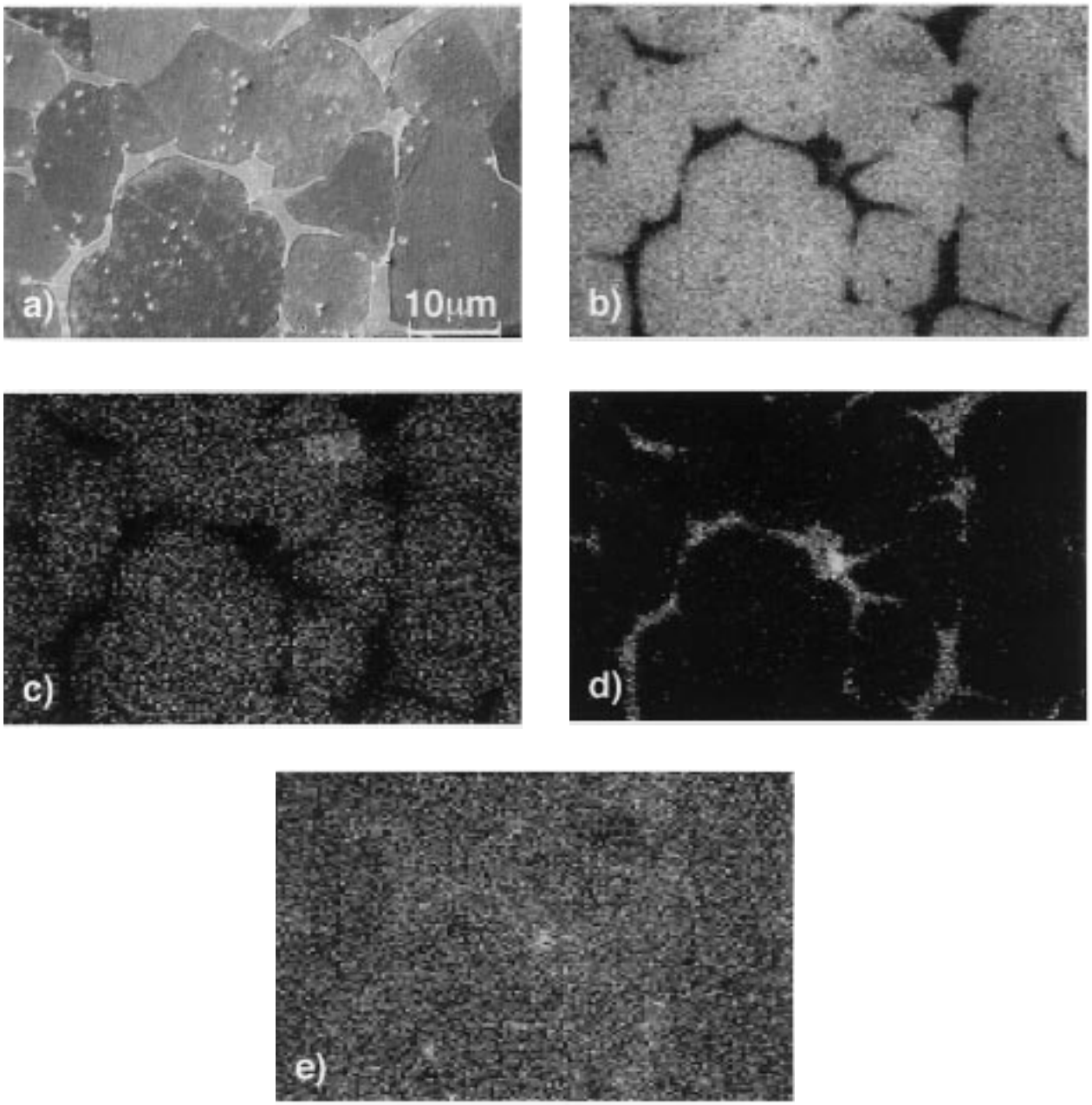

Figure 3 SAM images of the coarse Ti6A17Nb native oxide layer (information depth: 3–10 nm); (a) secondary electron image of the analyzed area; (b) SAM map of Ti, (c) Al, (d) Nb and (e) C.

therefore effects due to chemical modifications (e.g. dissolution) can be excluded. Friction force differences between the areas above α- and β-phases at different pH values are clearly visible and indicate locally different surface charges [14, 15]. Qualitatively, the following frictional force behavior in the two different oxide phase regions was detected: at pH 6.9 nearly no significant difference of friction force was observed between the two phases, while at pH 3.8 and pH 7.9 a slightly higher friction force was detected on the α-phase. At all pH values, however, the differences are small, indicating a surface charge distribution that is nearly homogeneous. The observed difference in the friction force signal between the α- and β-phase is, although optically clearly visible in the images, below 3%, i.e., very low in all cases.

The lateral surface composition determines the observed overall isoelectric point (IEP) if the area probed by the tip, while in contact during scanning, is homogeneously composed of the different oxides. The IEP of a material that is a mixture of different oxides is therefore determined both by the IEPs and by the charge densities of the different contributing oxides. The observed small differences are likely to be due to the different compositions of the α-and β-phases. These phases are laterally homogeneous, at least down to submicrometer (0.1 µm) scale, based on the scanning Auger results. It is likely that the tip, while scanning across the surface, will then sense a charge distribution that is an average of the different contributing oxides. In a recent investigation, it was shown that the lateral force between an AFM tip and an oxide surface in an electrolyte resembles a bell-shaped curve with a maximum between the IEPs of the materials under

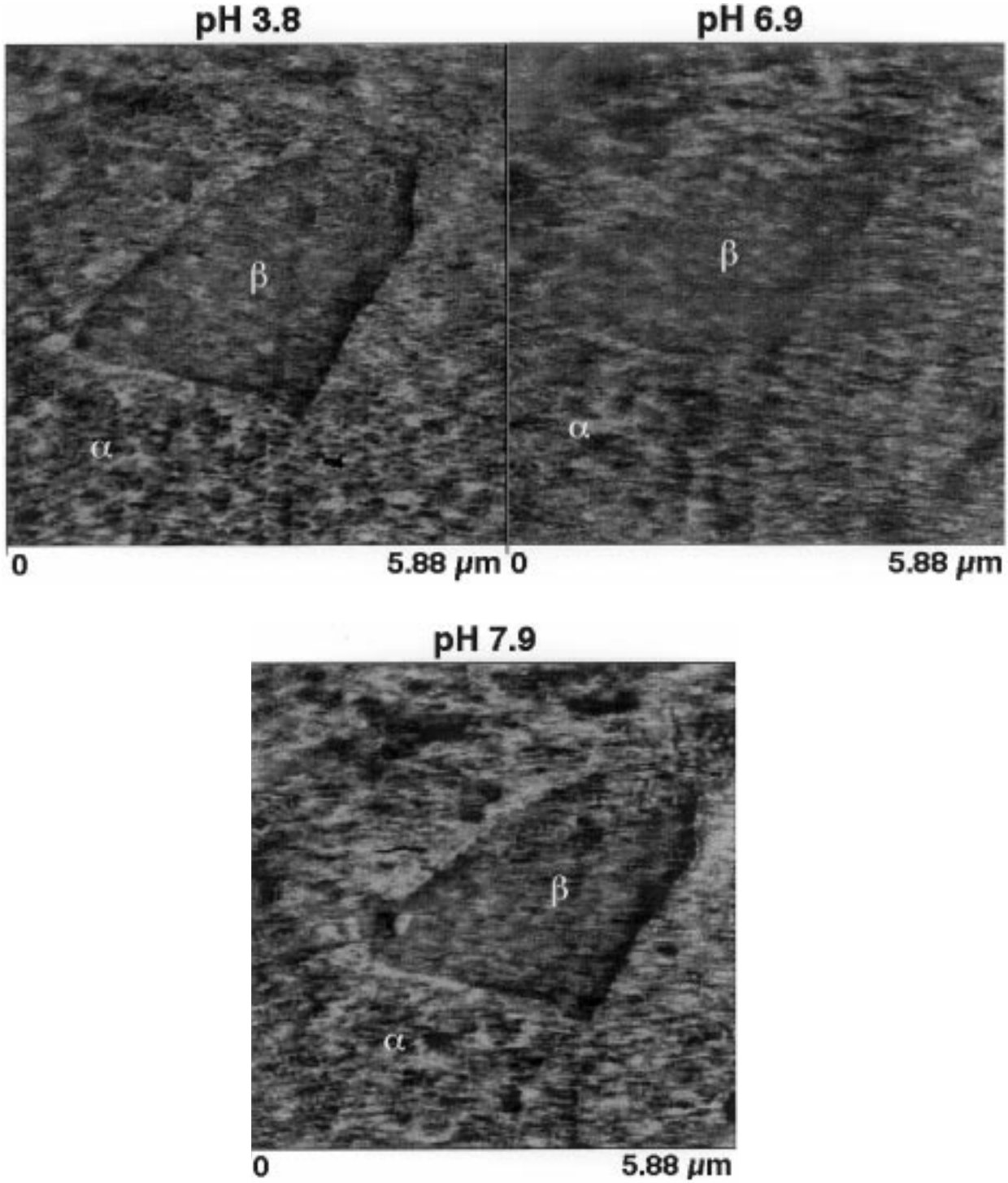

Figure 4 Friction force images at different pH values of coarse Ti6Al7Nb surfaces.

investigation and low values above and below both IEPs [14, 15]. We have modeled the lateral force on the α- and β-phases by taking into account the Al, Ti, and Nb oxide phases of the substrate and the Si_3N_4 tip. We have used gaussians with the maximum value between the IEPs of tip and each oxide and ''low'' values at both IEPs (the full-width-at-half-maximum corresponds to half of the difference between the IEPs). Literature values for the IEP of TiO_2 are reported to be in a range of 5 to 7 [19, 20], for Al_2O_3 around 8, and for Nb_2O_5 around 4.1 [20]. The IEP of an oxygen-plasma-cleaned tip is around 3. The maximum values are determined by the charge density, which is similar for Ti and Al [21], while for Nb no literature values are reported. It is reported, however, that specific adsorption of Na occurs on Nb_2O_5 in a NaCl solution for pH values above 4 [22]. The overall curve for each phase is then a superposition of these single curves. These overall curves representing the pH-dependence of the lateral force are slightly different for both phases, due to their different compositions (see Figs 5 and 6). For the calculation we have assumed highest surface charge density on TiO_2, a slightly lower density on Al_2O_3 ($\sim$ 80% of the value of Ti O_2) and $\sim$ 10% for Nb_2O_5.

Depending on the exact values of IEP, charge density and local composition of the different phases, the average lateral force will vary. However, since the composition of

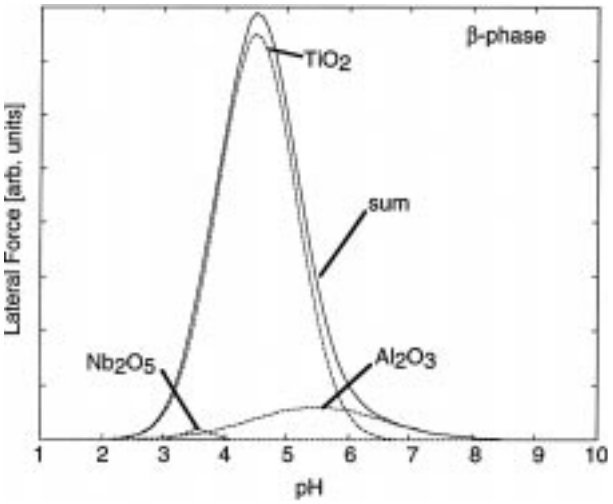

Figure 5 Expected lateral force for the different oxides on the β-phase and the resulting overall force.

the oxides on the α- and β-phase are similar, only small differences in lateral force will result. This is indeed supported by the small differences observed in the LFM measurements.

Our simple model predicts small differences over the entire pH range with only slight variations. The lower value at pH 7 is, however, not reflected in our simple model. However, it is not clear, for example, what effect a specific adsorption of Na ions on Nb_2O_5 will have on the entire system. A composition of the oxides that differs locally from the assumed stoichiometric ratios would also certainly modify the charge distribution. The lateral composition of the oxides may also play a crucial role. The assumption of small areas composed of the ideal oxides may be erroneous. Also it has to be borne in mind that LFM probes only the outermost layer, where an enrichment of some metal oxides might occur. A slight enrichment of Al in the β-phase, for example, would result in a lower friction force for pH $\sim$ 7. These LFM measurements indicate, however, that the physico-chemical properties of the outermost atomic layer of the two oxide phases are slightly different.

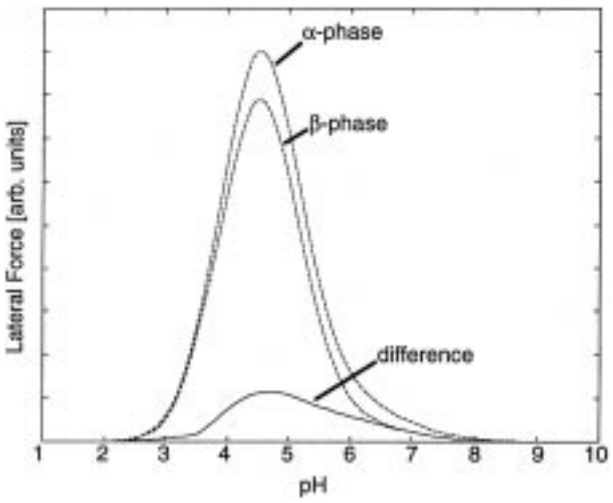

Figure 6 pH dependent lateral forces on α- and β-phase and their difference.

4. Conclusions

The surface of the implant alloy Ti6A17Nb is shown by X-ray photoelectron spectroscopy and scanning Auger microscopy to have a laterally inhomogeneous natural oxide film with a local composition that reflects the underlying duplex α-β-microstructure of the alloy. The oxide layer above the α-phase is enriched in Al by a factor of two, compared to the oxide above the β-phase, while the oxide above the β-phase has a sixfold higher Nb content compared to the oxide film above the α-phase. Lateral force measurements in an electrolyte, taken as a function of pH, indicate slight differences in the pH-dependence of the frictional force on the two oxide phases. It is proposed that these differences reflect different pH-dependent surface charges. It was shown that LFM has a very high sensitivity to differences in charge distribution.

Acknowledgment

The authors would like to thank: Mr M. Windler of Sulzer Orthopedics Ltd, CH-8404 Winterthur, for technical support and supply of materials; Dr P.-H. Vallotton and Mrs D. Müller of Straumann Institute, CH-4437 Waldenburg, for technical support and sample preparation; Mr R. Steger and Mr H. Weber of Sulzer Orthopedics Ltd for the microstructure analysis; Mr S. Kysela of Alusuisse Technology & Management AG, CH-8212 Neuhausen, for the microprobe analysis; and the Council of the Swiss Federal Institutes of Technology for their financial support of this work through their Priority Program on Materials.

References

1. S. G. STEINEMANN and P. -A. MÄUSLI, in Proceedings of the 6th World Conference on Titanium, France, 1988, (1989) p. 535.
2. J. LAUSMAA, L. MATTSSON, U. ROLANDER and B. KASEMO, *Biomed. Mater.* MRS; symposium (1986) p. 351.
3. B. KASEMO and J. LAUSMAA, *CRC Crit. Rev. Biocompatibility* **4** (1986) 335.
4. B. D. RATNER, in ''Surface characterisation of biomaterials,'' (Elsevier Science Publishers B.V., Amsterdam 1988) p. 13.
5. L. VROMAN and A. L. ADAMS, in ''Proteins at interfaces, physicochemical and biochemical studies,'' edited by J.L. Brash and T.A. Horbett (ACS, Washington DC, 1987) p. 154.
6. T. A. HORBETT and J. L. BRASH, in ''Proteins at interfaces, physicochemical and biochemical studies,'' edited by J.L. Brash and T.A. Horbett (ACS, Washington DC, 1987) p. 1.
7. X. CLIVAZ, R. EMCH, P. DESCOUTS, P. VAUDAUX, D. LEW, M. DELMI and H. VASEY, *Clin. Mater.* **5** (1990) 191.
8. T. ALBREKTSSON, P. -I. BRÅNEMARK, H. -A. HANSSON, B. KASEMO, K. LARSSON, I. LUNDSTRÖM, D. MCQUEEN and R. SKALAK, *Ann. Biomed. Eng.* **11** (1983) 1.
9. J. M. GOLD, M. SCHMIDT and S. G. STEINEMANN, in ''Clinical implant materials, advances in biomaterials'' vol. 9, edited by G. Heimke, U. Soltèsz and A.J.C. Lee (Elsevier Science Publishers B.V., Amsterdam 1990) p. 69.
10. R. THULL, *Med. Progr. Technol.* **16** (1990) 225.
11. J. E. DAVIES, in ''Surface characterization of biomaterials,'' edited by B.D. Ratner (Elsevier Science Publishers B.V., Amsterdam 1988) p. 219.
12. J. E. DAVIES, B. CAUSTON, Y. BOVELL, K. DAVY and C. S. STURT, *Biomaterials* **7** (1986) 231.
13. M. SEMLITSCH, F. STAUB and H. WEBER, *Biomedizinische Technik* **30** (1985) 334.
14. A. MARTI, G. HÄHNER and N. D. SPENCER, *Langmuir* **11** (1995) 4632.

15. G. HÄHNER, A. MARTI and N. D. SPENCER, *Trib. Lett.* **3** (1997) 359.
16. H. V. BOENIG, in ''Fundamentals of plasma chemistry and technology,'' (Technomic Publishing Company Inc., Lancaster, 1988).
17. S. EVANS, R. G. PRITCHARD and J. M. THOMAS, *J Electr. Spectrosc. Relat. Phenom.* **14** (1978) 341.
18. D. BRIGGS and M. P. SEAH, in ''Practical surface analysis,'' 2nd edn, vol 1 (John Wiley & Sons, Chichester, Salle + Sauerländer, Aarau, 1990) p. 247.
19. G. D. PARFITT, *Prog. Surf. Membrane Sci.* **11** (1976) 181.
20. G. A. PARKS, *Chem. Rev.* **65** (1965) 177.
21. T. W. HEALY and L. R. WHITE, *Adv. Colloid Interface Sci.* **9** (1978) 303.
22. M. KOSMULSKI, *Langmuir* **13** (1997) 6315.

Received 1 June
and accepted 20 July 1998